Research Article

Nano Research
2023, 16(8): 11358–11365

ISSN 1998-0124 CN 11-5974/O4
https://doi.org/10.1007/s12274-023-5813-9

Cobalt single atoms supported on monolithic carbon with a hollow-on-hollow architecture for efficient transfer hydrogenations

Xiangyi Gong[1,2], De-Chang Li[2] (✉), Qian Zhang[2,3], Wenquan Wang[2,3], Zhengbin Tian[2], Ge Su[1], Minghua Huang[1] (✉), and Guang-Hui Wang[2,3] (✉)

[1] *School of Materials Science and Engineering, Ocean University of China, Qingdao 266100, China*
[2] *Qingdao Institute of Bioenergy and Bioprocess Technology, Chinese Academy of Sciences, Qingdao 266101, China*
[3] *University of Chinese Academy of Sciences, Beijing 100049, China*

Received: 28 February 2023 / **Revised:** 3 May 2023 / **Accepted:** 6 May 2023

ABSTRACT

Single-atom catalysts (SACs) have received considerable attention in hydrogenation of nitroaromatic compounds to aromatic amines. In order to enhance the exposure of single atoms and overcome the mass transfer limitation, construction of hierarchical porous supports for single atoms is highly desirable. Herein, we report a straightforward method to synthesize Co single-atoms supported on a hollow-on-hollow structured carbon monolith (Co_1/HOHC-M) by pyrolysis of α-cellulose monolith loaded with PS-core@ZnCo-zeolite imidazolate frameworks-shell nanospheres (PS@Zn-ZIFs/α-cellulose). The hollow-on-hollow structure consists of a large hollow void with a diameter of ~ 290 nm (derived from the decomposition of polystyrene (PS) nanospheres) and a thin shell with hollow spherical pores with a diameter of ~ 10 nm (derived from the evaporation of ZnO nanoparticles that are *in-situ* formed during pyrolysis in the presence of CO_2 from α-cellulose decomposition). Benefitting from the hierarchically porous architecture, the Co_1/HOHC-M exhibits excellent catalytic performance (reaction rate of 421.6 mmol·g_{Co}^{-1}·h^{-1}) in the transfer hydrogenation of nitrobenzene to aniline, outperforming the powdered sample of Co_1/HCS without the hollow spherical mesopores (reaction rate of 353.8 mmol·g_{Co}^{-1}·h^{-1}). It is expected that this strategy could be well extended in heterogeneous catalysis, given the wide applications of porous carbon-supported single-atom catalysts.

KEYWORDS

hollow-on-hollow, Co single-atoms, nitrobenzene, transfer hydrogenation

1 Introduction

Aromatic amines, which are important intermediates in the fine-chemical industry for manufacturing chemicals (such as pharmaceuticals, polymers, agrochemicals, and dyes) are generally obtained by selective hydrogenation of nitro-compounds [1–3]. However, the traditional hydrogenation processes are often problematic, due to the use of environmentally harmful organic solvents and/or high-pressured hydrogen [4, 5]. Instead, selective transfer hydrogenation using isopropyl alcohol as a hydrogen donor, has received significant attention, owing to its features of good catalytic efficiency, high atomic economy, and simple operability [6]. So far, numerous heterogeneous catalysts have been developed for the catalytic transfer hydrogenation reactions. Among them, the supported noble metal (such as Pd, Pt, and Au) catalysts are effective [7–9], but their high cost and poor catalytic selectivity make them unsuitable for large-scale applications. Non-precious metal (such as Fe, Co, and Ni) catalysts have emerged as appealing alternatives with relatively high selectivities [10], but they still suffer from issues such as low transformation efficiency and deactivation caused by sintering and leaching of metal species. Generally, the catalysts for selective transfer hydrogenation of nitro-compounds should own the following characteristics: i) highly active and selective catalytic sites to achieve an efficient transformation of nitro groups without affecting other reducible groups [11–13]; ii) hierarchically porous architecture to accelerate mass transfer and enhance the exposure of active sites [14, 15]; iii) robust macroscopic forms to ensure that they are easy to operate and reuse [16, 17].

Single-atom catalysts (SACs) with unique electronic and geometric properties (e.g., Fe_1/N-C [6], Co SSCs@NG [18], and Ni-SAs/NC [19]), have received considerable attention in the past decade, due to their enhanced catalytic performances in a wide scope of industrially important reactions [20–30], especially in the selective hydrogenation of nitro-compounds. Among various approaches for SACs synthesis, pyrolysis of zinc-metal bimetallic zeolite imidazolate frameworks (ZIFs) is an efficient method to prepare single atoms uniformly dispersed on a porous carbon [31–37]. During pyrolysis, along with the formation of N-doped carbon (NC) and the evaporation of Zn atoms, the spatially separated metal atoms are tightly anchored by the N species derived from organic linkers of ZIFs to form a single atomic M-NC (M = Fe, Co, and Ni) structure [38–41]. The catalytic performance of these M-NC materials is highly dependent on the exposure of active sites and internal mass transfer [42–48]. However, most ZIFs-derived catalysts have a considerable portion of the metal sites buried in the carbon matrix, which inevitably reduces the utilization efficiency of metal atoms [49]. It is therefore

Address correspondence to De-Chang Li, lidc@qibebt.ac.cn; Minghua Huang, huangminghua@ouc.edu.cn; Guang-Hui Wang, wanggh@qibebt.ac.cn

necessary to increase the accessibility of active sites through rational design of the porous structure of carbon matrix. Among numerous architectures for supporting SACs, a hollow structure featuring two-sided available surfaces and a large void represents one of the most effective architectures [50–53], but it is usually synthesized in powder form. To improve the flexibility in practical applications, the powdery catalysts are typically shaped into monolithic forms with binders or high pressure, which further hinders the internal mass transfer and the exposure of active sites [54–57]. Therefore, in order to maximize the advantage of the hollow structure within a shaped catalyst, it is desired to fabricate the hollow structures in a preformed monolith, rather than shaping the hollow materials via the post-processing strategy. However, the former strategy is rarely reported.

Herein, we demonstrate a straightforward strategy for synthesizing Co single-atoms supported on a hollow-on-hollow structured carbon monolith (Co_1/HOHC-M) by pyrolysis of α-cellulose monolith loaded with PS-core@ZnCo-ZIFs-shell nanospheres (PS@ZnCo-ZIFs/α-cellulose). The hollow-on-hollow structure consists of a large hollow void (~ 290 nm) derived from the decomposition of polystyrene (PS) nanospheres and a thin shell with hollow spherical pores (~ 10 nm) after the evaporation of ZnO nanoparticles (*in-situ* formed during pyrolysis in the presence of CO_2 from α-cellulose decomposition). Such hierarchically porous carbon monolith is expected to provide well-developed channels for mass transfer and abundant surfaces to expose the active sites. It is found that the Co_1/HOHC-M exhibits superior catalytic performance in the transfer hydrogenation of nitrobenzene to aniline, outperforming the control sample without the hollow spherical pores (Co_1/HCS). The Co_1/HOHC-M can also be extended to selectively catalyze other nitroarenes with different substituted functional groups.

2 Experimental

2.1 Preparation of carboxylate-terminated PS spheres

The PS spheres were prepared according to the previously reported method [48]. In a typical synthesis, 21 mL of styrene, 1.1 mL of methyl methacrylate, 0.92 mL of acrylic acid, and 0.49 g of NH_4HCO_3 were added to 100 mL of deionized water in a 250 mL round bottom flask under mechanical stirring. When the solution reached a temperature of 70 °C, 0.53 g of ammonium persulfate was added, and continued to react for 12 h at 80 °C. The obtained white product was collected by centrifugation and washed with methanol for several times. The synthesized sample was re-dispersed in methanol for further use.

2.2 Preparation of PS@ZnCo-ZIFs core–shell composites

Typically, 300 mg of PS spheres and 20 mmol of 2-methylimidazole were added into 40 mL of methanol and mixed under ultrasonic treatment for 15 min. Subsequently, 40 mL of methanol solution containing 2 mmol of Zn/Co nitrates with molar ratios of 20/1 was added slowly. After stirring at 70 °C for 1 h, the obtained precipitates were centrifuged, washed thoroughly with methanol. The synthesized sample was re-dispersed in methanol with a concentration of 10 mg·mL^{-1}.

2.3 Preparation of PS@ZnCo-ZIFs/α-cellulose

600 mg of α-cellulose was added into 120 mL of methanol containing PS@ZnCo-ZIFs and stirred vigorously for 6 h. The purple product was collected by filtration, washed thoroughly with methanol, and finally dried at 60 °C for 10 h. For comparison, PS@Zn-ZIFs/α-cellulose without Co addition was also synthesized according to the above procedure.

2.4 Preparation of Co_1/HOHC-M

220 mg of PS@ZnCo-ZIFs/α-cellulose was directly pressed into a tablet by a pellet press under a mild pressure (1.0 bar) and pyrolyzed at 920 °C under Ar flow (100 mL·min^{-1}). The thermal reduction procedure was as follows: The sample was heated to 920 °C with a rate of 2 °C·min^{-1} and maintained at 920 °C for 2 h. After cooling down to room temperature in Ar atmosphere, the sample of Co_1/HOHC-M was obtained. For comparison, control samples were prepared by using PS@Zn-ZIFs/α-cellulose tablet, PS@ZnCo-ZIFs powder, PS@ZnCo-ZIFs tablet, α-cellulose, and PS/α-cellulose as precursors, respectively, under the same pyrolysis conditions as that of Co_1/HOHC-M.

2.5 Preparation of PS@ZnCo-ZIFs-CO_2-500

The PS@ZnCo-ZIFs were placed in a porcelain boat, and then transferred into a quartz tube. A three-port flask containing 60 mL of sulfuric acid (0.5 M) and a gas drying device was connected to the inlet-end of the quartz tube. The sample was heated to 500 °C with a rate of 2 °C·min^{-1} under Ar flow and maintained at 500 °C for 2 h. When the temperature reached 300 °C, 40 mL of sodium carbonate solution (0.14 M) was slowly injected into the sulfuric acid solution to generate CO_2, which, after drying, flows across the quartz tube. After cooling down to room temperature, the sample of PS@ZnCo-ZIFs-CO_2-500 was obtained.

2.6 Catalysis evaluation

The transfer hydrogenation performance of catalysts was measured in a 25 mL autoclave reactor with a reaction solution containing 0.25 mmol of nitrobenzene, a certain amount of catalyst, and 10 mL of isopropyl alcohol. The reactor was sealed, pressurized with 1 MPa of N_2, and then heated to 150 °C. After reaction for a certain period of time, the reactor was cooled down rapidly to room temperature in an ice/water bath. The products were analyzed by gas chromatography (GC) (Agilent 7890B) and gas chromatography-mass spectrometry (GC-MS) (Agilent 7890B-5977B). O-xylene was used as an internal standard to quantitatively analyze the concentration of each component. The catalyst was recovered after reaction, washed with ethanol (30 mL), dried under vacuum oven at 80 °C, and then reduced at 400 °C under 10% H_2/Ar flow.

3 Results and discussion

3.1 Preparation and characterization of Co_1/HOHC-M

The synthetic strategy for Co_1/HOHC-M is schematically depicted in Scheme 1. First, carboxylic acid-modified PS nanospheres with an average size of ~ 380 nm (Fig. S1(a) in the Electronic Supplementary Material (ESM)) were synthesized according to the method reported previously [48]. Then, the ZnCo-ZIFs were coated on the surface of PS nanospheres to form the PS-core@ZnCo-ZIFs-shell structure (Figs. S1(b) and S2 in the ESM). Next, the PS@ZnCo-ZIFs were loaded onto the α-cellulose and shaped into a tablet under a mild pressure (1.0 bar). Scanning electron microscopy (SEM) images show that the spherical PS@ZnCo-ZIFs composites are densely distributed on the surface of α-cellulose (Figs. S1(c) and S1(d) in the ESM). The powder X-ray diffraction (XRD) pattern confirms the formation of ZIFs in the PS@ZnCo-ZIFs/α-cellulose composite (Fig. S3 in the ESM). At last, the Co_1/HOHC-M was obtained by pyrolysis of PS@ZnCo-ZIFs/α-cellulose composite at 920 °C under an Ar flow, which still retains the tablet shape but with about 20% shrinkage (Fig. 1(a)).

According to the SEM images captured on the cross section of the Co_1/HOHC-M tablet, abundant macropores exist among the stacked carbon rods derived from α-cellulose (Fig. S4 in the ESM),

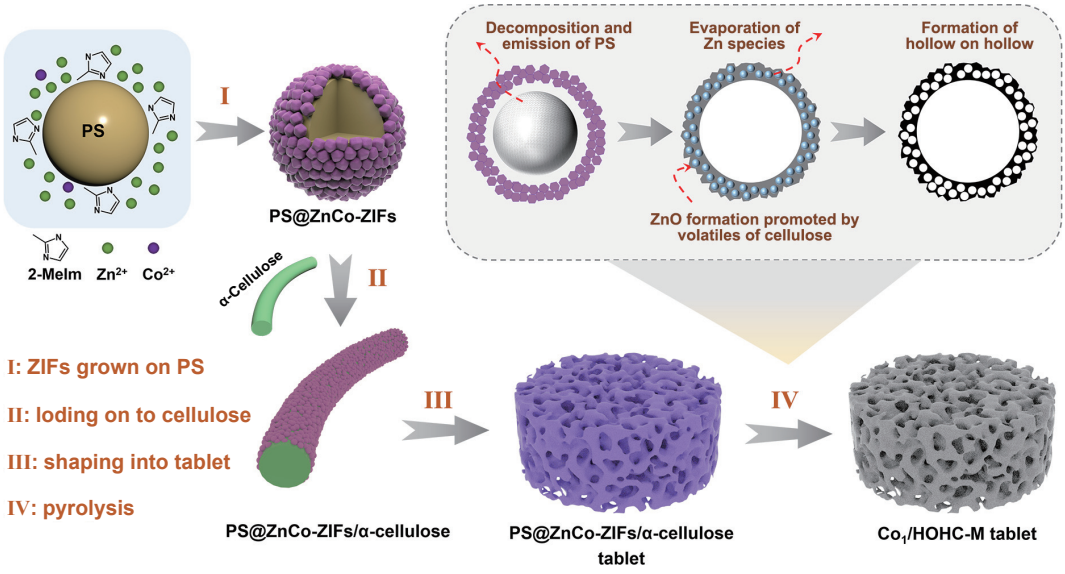

Scheme 1 Schematic illustration for the fabrication of Co_1/HOHC-M.

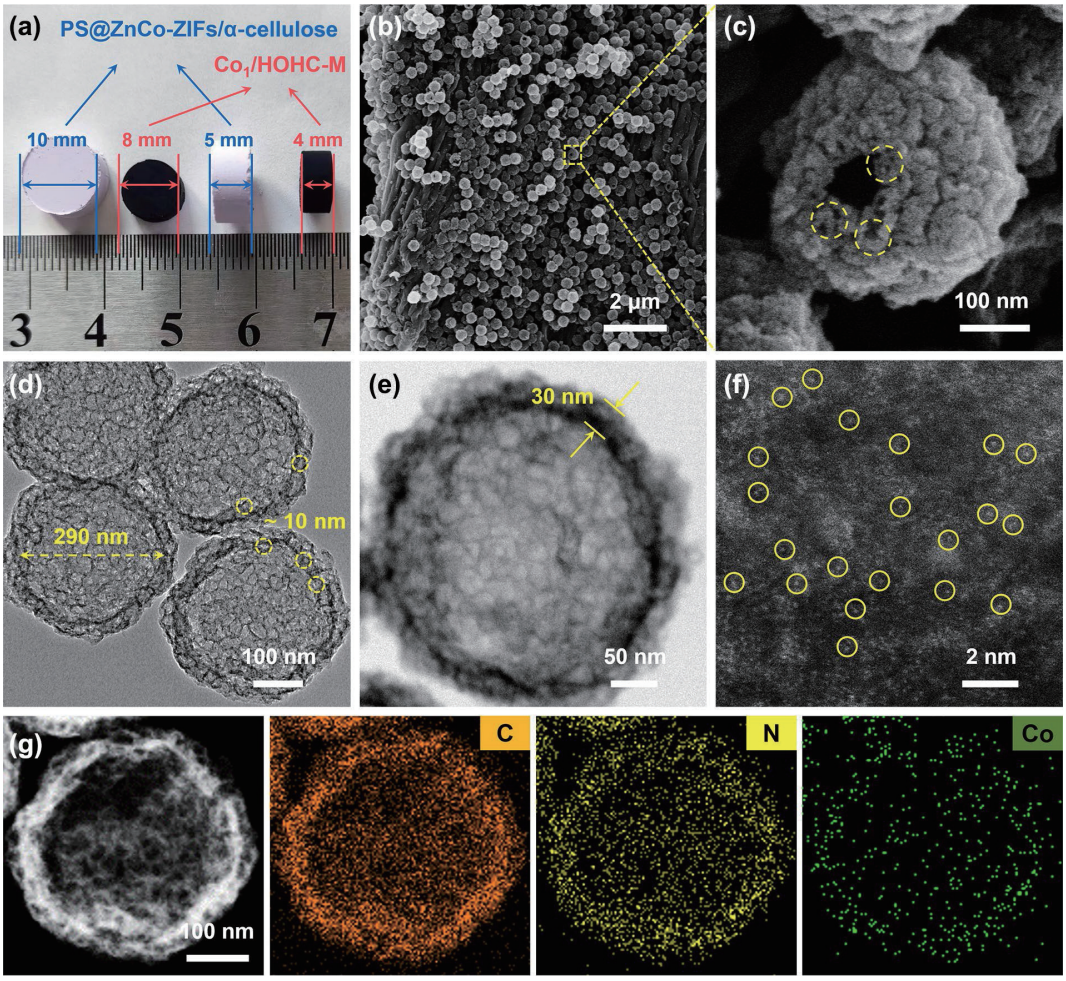

Figure 1 (a) Photograph of the shaped catalyst before and after pyrolysis. ((b) and (c)) SEM and ((d) and (e)) HRTEM images of Co_1/HOHC-M. The smaller hollow cavities are marked with yellow circles. (f) Aberration-corrected HAADF-STEM image of Co_1/HOHC-M. The Co atoms are marked with yellow circles. (g) HAADF-STEM and the corresponding elemental mapping images of Co_1/HOHC-M.

which could be beneficial for mass transfer during catalysis. The carbon spheres derived from PS@ZnCo-ZIFs are still uniformly grafted on the surface of carbon rods (Fig. 1(b)), and the hollow structure can be observed from the broken spheres (Fig. 1(c)). According to the transmission electron microscopy (TEM) images (Figs. 1(d) and 1(e) and Fig. S5 in the ESM), the Co_1/HOHC-M has a hollow-on-hollow structure, i.e., a hollow cavity (~ 290 nm) delimited by a thin shell (~ 30 nm) with hollow spherical pores (~ 10 nm). The high-angle annular dark-field scanning transmission electron microscopy (HAADF-STEM) and energy-dispersive X-ray spectroscopy (EDX) mapping images of Co_1/HOHC-M reveal that the C, N, and Co elements are uniformly distributed on the hollow shell without any metal nanoparticles being observed (Fig. 1(g)). The discrete bright dots in the aberration-corrected HAADF-STEM images (Fig. 1(f) and Fig. S6 in the ESM) demonstrate the atomic dispersion of Co atoms.

XRD pattern of Co_1/HOHC-M exhibits two broad peaks at around 26° and 43° indexing to amorphous carbon (Fig. 2(a)) [58, 59], and no distinctive peaks belonging to crystalline metal species are detected. According to inductively coupled plasma optical emission spectroscopy (ICP-OES), the Co loading amount in the Co_1/HOHC-M is ~ 2.41 wt.% (Table S1 in the ESM), and the atomic ratio of Zn/Co is 0.89 (much lower than the value of 20/1 used in synthesis), indicating that the majority of Zn has been evaporated after pyrolysis. X-ray absorption near-edge structure (XANES) and EXAFS measurements were employed to elucidate the coordination environment and valence state of the Co species in Co_1/HOHC-M. The standard spectra of Co foil, CoO, and Co_3O_4 were used as references. As shown in Fig. 2(b) and Fig. S7 in the ESM, the Co K-edge of Co_1/HOHC-M is close to that of CoO and lower than that of Co_3O_4, indicating that Co atoms in Co_1/HOHC-M are positively charged with average valence state of about +2. The Fourier transform (FT) k^3-weighted EXAFS spectra of Co_1/HOHC-M (Fig. 2(c) and Fig. S8 in the ESM) show only a main peak at about 1.4 Å, which corresponds to the first coordination shell of Co–N [60, 61]. The Co–Co and Co–O coordination peaks are not observed, confirming the atomic dispersion of Co. Furthermore, EXAFS fittings were carried out to obtain the structural parameters and extract the quantitative chemical configuration of Co atoms in Co_1/HOHC-M (Table S2 in the ESM). The corresponding EXAFS fitting curves of Co_1/HOHC-M in the *R* space and *k* space (Fig. 2(d) and Fig. S9 in the ESM) reveal that the coordination number of Co in the Co_1/HOHC-M is ~ 4, suggesting that Co atom is coordinated to four N atoms in the Co_1/HOHC-M. All of these results demonstrate that Co is atomically dispersed in the Co_1/HOHC-M, in good agreement with the aberration-corrected HAADF-STEM results (Fig. 1(f) and Fig. S6 in the ESM).

The X-ray photoelectron spectroscopy (XPS) analysis (Fig. S10 in the ESM) further demonstrates the existence of C, N, and Co elements in Co_1/HOHC-M. The C 1s spectra can be divided into C–C (284.6 eV), C–N (285.2 eV), C–O (286.3 eV), and C=O (288.6 eV), and the existence of C–N bond confirms that N atoms have been doped in the carbon skeletons (Fig. S11(a) in the ESM). In the Co 2p high-resolution spectra of Co_1/HOHC-M (Fig. S11(b) in the ESM), the peaks at 780.6 and 796.0 eV, accompanied by two satellite peaks at 784.6 and 803.8 eV, are typical feature for Co^{2+}. The valence state of Co is in good agreement with the result in XAS analysis. The N 1s XPS spectra of Co_1/HOHC-M can be deconvolved as pyridinic-N (398.6 eV), pyrrolic-N (400.1 eV), graphitic-N (401.2 eV), and oxidized N (403.1 eV) species, respectively (Fig. S11(c), Tables S3 and S4 in the ESM). For comparison, PS@ZnCo-ZIFs without α-cellulose addition were pyrolyzed under the same conditions, and the obtained sample was denoted as Co_1/HCS. According to the SEM (Figs. S12(a) and S12(b) in the ESM) and TEM images (Fig. S12(c) in the ESM) of Co_1/HCS, only the hollow carbon spheres derived from PS-template are observed, without hollow spherical pores in the hollow shells, which is different from that of Co_1/HOHC-M. The porous structures of Co_1/HOHC-M and Co_1/HCS were further characterized by N_2 sorption. The samples of Co_1/HOHC-M and Co_1/HCS display type IV and type I isotherms, respectively (Fig. 2(e)). The hysteresis loop closed at $P/P_0 \approx 0.42$ for Co_1/HOHC-M is pronounced (characteristic of mesoporous hollow structure [62]), whereas that for Co_1/HCS is negligible, indicating a visible difference in their porous structures. According to the pore size distributions of Co_1/HOHC-M and Co_1/HCS (Fig. 2(f)), an obvious peak centred at ~ 10 nm appears in Co_1/HOHC-M, but not in Co_1/HCS. It can be inferred that the formation of pores with a size of ~ 10 nm is related to the addition of α-cellulose during synthesis. The Brunner–Emmet–Teller (BET) surface area of Co_1/HOHC-M is 463.3 $m^2 \cdot g^{-1}$, being lower than that of Co_1/HCS (575.7 $m^2 \cdot g^{-1}$) (Table S5 in the ESM), probably due to the less porosity of α-cellulose-derived carbon in Co_1/HOHC-M. It is expected that the hierarchically porous structure of Co_1/HOHC-M will undoubtedly be beneficial for exposure of the active sites and mass transfer of substrates.

3.2 Formation mechanism of Co_1/HOHC-M

The structural evolution of different samples in pyrolysis was tested by a thermo-gravimetric (TG) analyzer (Fig. S13 in the ESM). The decomposition temperatures for α-cellulose and PS-template are ~ 350 and ~ 450 °C, respectively (Fig. 3(a)). For PS@ZnCo-ZIFs, two derivative thermogravimetry (DTG) peaks at ~ 450 and ~ 650 °C are observed (Fig. 3(a)), which can be assigned to the decompositions of PS-template and ZnCo-ZIFs, respectively. However, the DTG curve of PS@ZnCo-ZIFs/α-cellulose only shows two peaks at ~ 350 and ~ 450 °C, without the

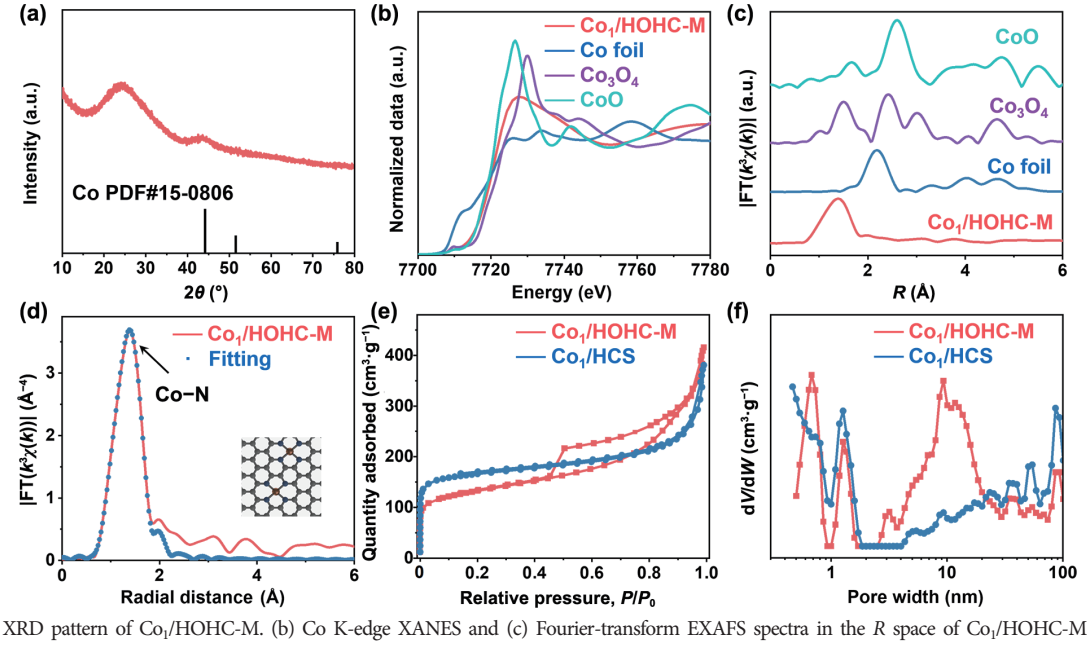

Figure 2 (a) XRD pattern of Co_1/HOHC-M. (b) Co K-edge XANES and (c) Fourier-transform EXAFS spectra in the *R* space of Co_1/HOHC-M and reference samples. (d) Corresponding EXAFS fitting curves of Co_1/HOHC-M in *R* space (inset: the model of Co_1/HOHC-M). (e) N_2 sorption isotherms and (f) pore-size distributions of Co_1/HOHC-M and Co_1/HCS.

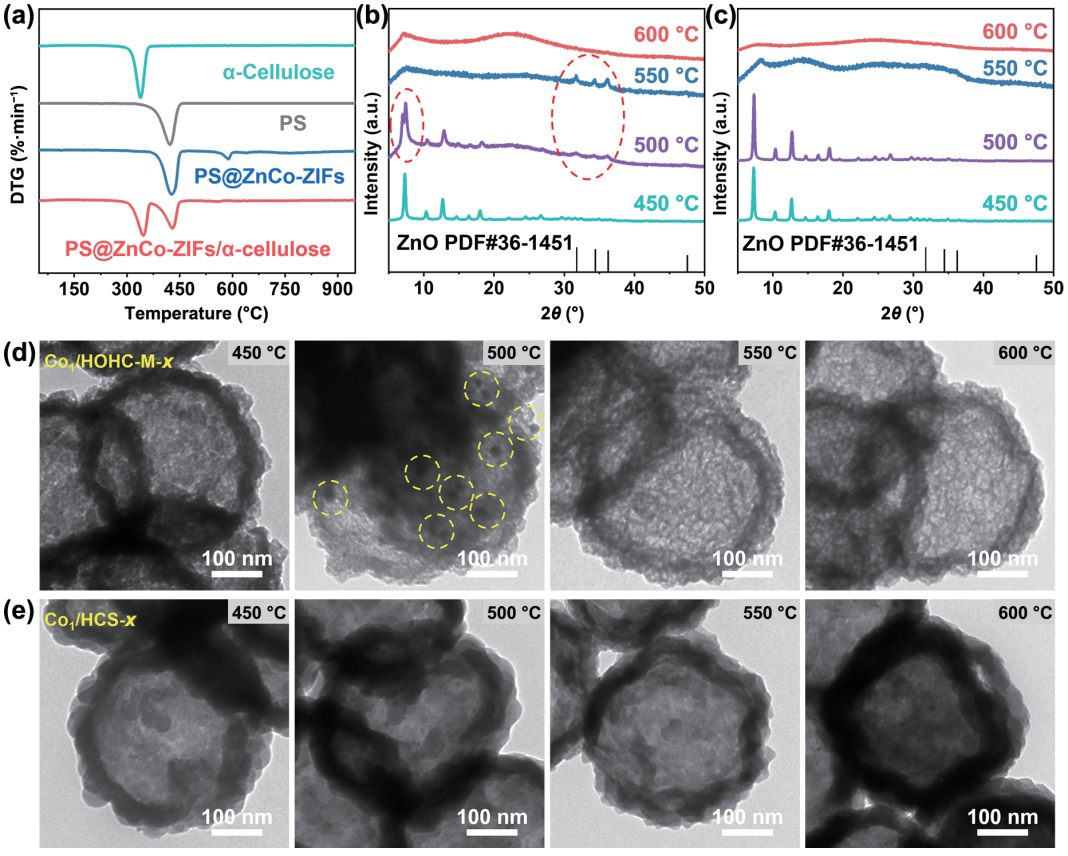

Figure 3 (a) DTG curves of α-cellulose, PS, PS@ZnCo-ZIFs, and PS@ZnCo-ZIFs/α-cellulose. XRD patterns of (b) Co_1/HOHC-M-*x* and (c) Co_1/HCS-*x* (*x* = 450, 500, 550, and 600 °C). TEM images of (d) Co_1/HOHC-M-*x* and (e) Co_1/HCS-*x* (*x* = 450, 500, 550, and 600 °C).

peak (~ 650 °C) attributed to ZnCo-ZIFs decomposition (Fig. 3(a)). It is possible to infer that the volatiles from α-cellulose decomposition might boost the ZnCo-ZIFs collapse at a relatively low temperature. Based on the TG analysis, we then attempted to tailor the pyrolysis temperature of PS@ZnCo-ZIFs/α-cellulose and PS@ZnCo-ZIFs to capture the corresponding intermediates (denoted as Co_1/HOHC-M-*x* and Co_1/HCS-*x*, respectively; *x* = 450, 500, 550, and 600 °C). As exhibited by XRD patterns (Figs. 3(b) and 3(c)), the diffraction peak at ~ 7.3° (belonging to ZnCo-ZIFs) for Co_1/HOHC-M-500 is much broader than that for Co_1/HCS-500, and new diffraction peaks at 31.7°, 34.4°, and 36.2° for Co_1/HOHC-M-500 start to appear, which can be indexed to (100), (002), and (101) diffraction planes of ZnO (JCPDS No. 36-1451). These results suggest that the crystal structure of ZnCo-ZIFs in Co_1/HOHC-M-500 is more prone to be destroyed than in Co_1/HCS-500. When the temperature is elevated to 550 °C, the diffraction peaks belonging to ZnCo-ZIFs disappear for both samples of Co_1/HOHC-M-550 and Co_1/HCS-550. However, there are still no ZnO peaks for Co_1/HCS-550 (Fig. 3(c)). As the temperature is further raised to 600 °C, only two broad peaks that belong to amorphous carbon exist in both samples of Co_1/HOHC-M-600 and Co_1/HCS-600.

Next, TEM images of Co_1/HOHC-M-*x* and Co_1/HCS-*x* were acquired to visualize the structural evolution process. As shown in Figs. 3(d) and 3(e), the PS-template is completely volatilized for both of Co_1/HOHC-M-450 and Co_1/HCS-450, leaving behind a large hollow void. Compared with Co_1/HOHC-M-450, numerous nanoparticles appear in the shell of Co_1/HOHC-M-500 (Fig. 3(d)), which then disappeared and left the hollow spherical pores in the shell after increasing temperature to 550 °C (Co_1/HOHC-M-550) and 600 °C (Co_1/HOHC-M-600). In contrast, the morphologies of Co_1/HCS-*x* are almost unchanged during pyrolysis at temperatures ranging from 450 to 600 °C (Fig. 3(e)).

As reported in previous studies, a mass of CO_2 can be released from the pyrolysis of α-cellulose [63] and transformed into CO_3^{2-}/HCO_3^-, which facilitate the destruction of linkage between Zn and ligand through their competitive coordination to Zn cations [64] and lead to the formation of ZnO nanoparticles. To demonstrate the role of CO_2, we treated the PS@ZnCo-ZIF at 500 °C under CO_2 atmosphere (instead of the volatiles from α-cellulose) to obtain the sample of PS@ZnCo-ZIF-CO_2-500, which possesses a similar hollow structure with ZnO nanoparticles in the shell to the Co_1/HOHC-M-500 (Figs. S14 and S15 in the ESM). Therefore, we can propose the formation mechanism of the hollow-on-hollow structured Co_1/HOHC-M as follows. During pyrolysis, the PS nanospheres are decomposed to generate the large hollow void; CO_2 and other volatiles released from the cellulose decomposition weaken the linkage between Zn and ligand in ZIFs via ligand exchange, and result in the formation of ZnO nanoparticles at temperature of 450–550 °C; the ZnO nanoparticles are then sublimated at temperature above 550 °C, leaving behind numerous hollow spherical pores in the shell; during this period, the Co single atoms are very stable due to their strong interaction with N defects in the carbon skeleton.

3.3 Catalytic transfer hydrogenation reactions

The catalytic properties of the as-prepared samples were investigated by transfer hydrogenation of nitrobenzene to aniline using isopropanol as the H-donor. Firstly, using the α-cellulose-derived carbon or PS/α-cellulose-derived carbon as catalyst, the conversion of nitrobenzene is negligible (Table S6 in the ESM). However, a complete conversion of nitrobenzene with 96% selectivity towards aniline over Co_1/HOHC-M was achieved in 140 min (Fig. 4(a) and Table S6 in the ESM). By contrast, the conversion of nitrobenzene in 140 min is only 76% and 37% over Co_1/HCS-M (obtained by pyrolyzing the PS@ZnCo-ZIFs tablet) and HOHC-M (obtained by pyrolyzing the PS@Zn-ZIFs/α-

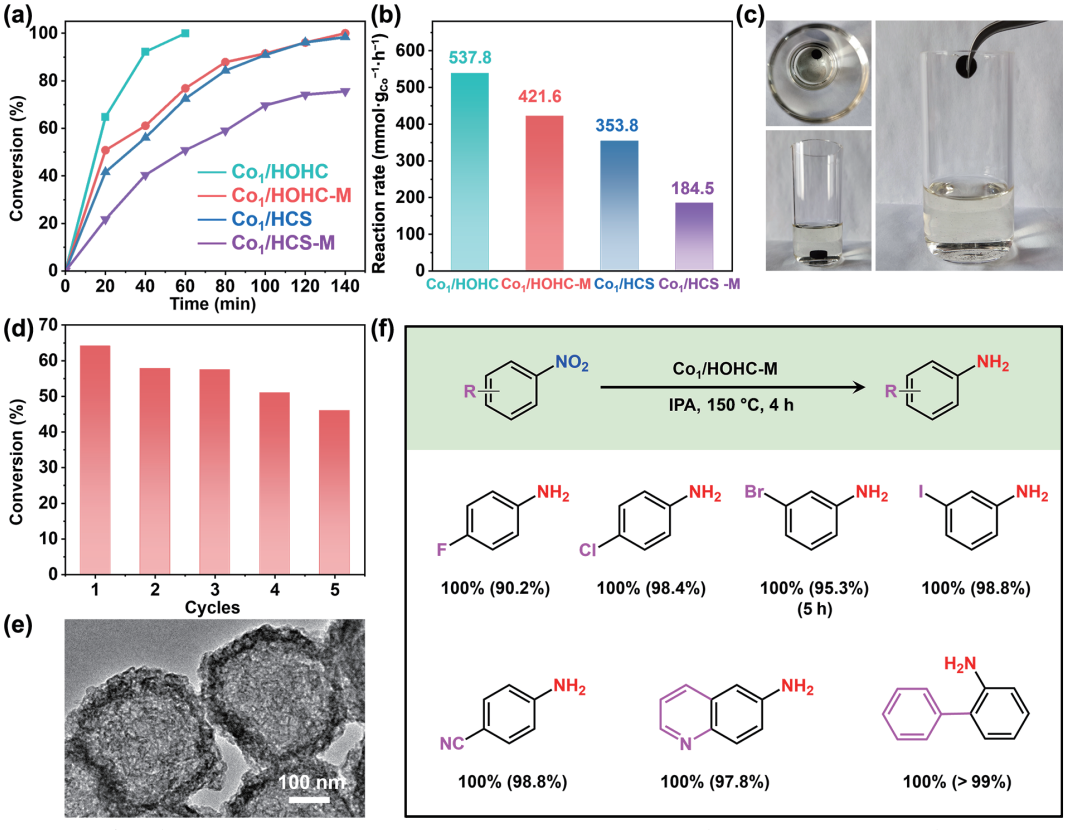

Figure 4 (a) Time courses of nitrobenzene conversion over Co_1/HOHC, Co_1/HOHC-M, Co_1/HCS, and Co_1/HCS-M. Reaction conditions: 0.25 mmol nitrobenzene, Co dosage of 1.5×10^{-2} mmol, 10 mL isopropyl alcohol, 150 °C, 1 MPa N_2. (b) The reaction rate in 20 min over Co_1/HOHC, Co_1/HOHC-M, Co_1/HCS, and Co_1/HCS-M, respectively. (c) Photographs of the catalyst separated with tweezers after the reaction. (d) Cycling stability of Co_1/HOHC-M catalyst for the reaction. Reaction conditions: 0.25 mmol nitrobenzene, Co dosage of 1.5×10^{-2} mmol, 10 mL isopropyl alcohol, 150 °C, 1 MPa N_2, 50 min. (e) TEM image of Co_1/HOHC-M catalyst after five rounds of usage. (f) Transfer hydrogenation of other nitro-compounds over Co_1/HOHC-M. Reaction conditions: 0.25 mmol nitrobenzene derivatives, Co dosage of 1.5×10^{-2} mmol, 10 mL isopropyl alcohol, 150 °C, 1 MPa N_2.

cellulose tablet) (Fig. S16 in the ESM), respectively. When using the powdery Co_1/HOHC and Co_1/HCS as catalyst, the nitrobenzene can be completely hydrogenated in 60 and 140 min, respectively. The reaction rates over Co_1/HOHC, Co_1/HOHC-M, Co_1/HCS, and Co_1/HCS-M were calculated as 537.8, 421.6, 353.8, and 184.5 mmol·g_{Co}^{-1}·h^{-1}, respectively. The higher catalytic efficiency of Co_1/HOHC-M than those of Co_1/HCS-M and Co_1/HCS (also being better than most catalysts reported in literature (Table S7 in the ESM) that use isopropanol as H donor) should be attributed to its hollow-on-hollow structure, which allows a high exposure of active sites and enhances the mass transfer. In addition, the Co_1/HOHC-M tablet can be easily separated from the liquid reaction system with negligible mass loss (Fig. 4(c)), which is convenient for recycling utilization. The Co_1/HOHC-M tablet was recycled for 5 times, and the conversion of nitrobenzene decreased from ~ 64% to ~ 46% (Fig. 4(d)), which is probably caused by the pore blockage that decreases the exposure of active sites. The XRD results show that the spent catalyst exhibits similar characteristic peaks to the fresh catalyst, and no characteristic peaks of Co appear (Fig. S17 in the ESM). Moreover, the hollow-on-hollow structure remained intact and Co atoms did not agglomerate into distinct particles according to the TEM image (Fig. 4(e)).

Next, the substrate scope of transfer hydrogenation of nitro-compounds over Co_1/HOHC-M was studied. As shown in Fig. 4(f) and Fig. S18 in the ESM, for halogen-substituted nitro-compounds (such as 1-fluoro-4-nitrobenzene, 1-chloro-4-nitrobenzene, 3-bromonitrobenzene, and 1-iodo-3-nitrobenzene), the nitro group was rapidly converted into amino group over Co_1/HOHC-M with ~ 100% conversion and > 90% selectivity (the majority of Ar-halogen bonds were preserved), indicating its good catalytic selectivity for nitro group. In addition, the reaction system using Co_1/HOHC-M as catalyst can be extended to other nitro-compounds, such as 4-nitrobenzonitrileas, 6-nitroquinoline, and 2-nitrobiphenyl, demonstrating its outstanding adaptability.

4 Conclusions

In summary, we have developed a facile strategy for synthesis of Co_1/HOHC-M by pyrolyzing the composite of PS@ZnCo-ZIFs/α-cellulose. The hollow-on-hollow spheres loaded on the α-cellulose-derived carbon contain a large hollow void (~ 290 nm, derived from the decomposition of PS-template) and a thin shell with hollow spherical pores (~ 10 nm, derived from the evaporation of ZnO nanoparticles). The existence of α-cellulose plays a key role in the formation of the hollow spherical pores, because CO_2 and other volatiles released from the cellulose decomposition result in the formation of ZnO nanoparticles. The hierarchically porous structure of Co_1/HOHC-M provides well-developed channels for mass transfer and abundant surfaces to expose the active sites. It has been found that the Co_1/HOHC-M shows an excellent catalytic performance for transfer hydrogenation of nitrobenzene to aniline, and can be extended to catalyze other nitroarenes with different substituted functional groups. This work provides a facile way to synthesize shaped single-atom catalysts with hierarchically porous structure, which have potential applications in various reactions.

Acknowledgements

This work was supported by the National Natural Science Foundation of China (No. 52100169) and the Natural Science

Foundation of Shandong Province (Nos. ZR2020QB196, ZR2022ZD30, and ZR2020QB053).

Electronic Supplementary Material: Supplementary material (associated with the details of characterization) is available in the online version of this article at https://doi.org/10.1007/s12274-023-5813-9.

References

[1] Zhang, L. L.; Zhou, M. X.; Wang, A. Q.; Zhang, T. Selective hydrogenation over supported metal catalysts: From nanoparticles to single atoms. *Chem. Rev.* **2020**, *120*, 683–733.

[2] Guan, Q. Q.; Zhu, C. W.; Lin, Y.; Vovk, E. I.; Zhou, X. H.; Yang, Y.; Yu, H. C.; Cao, L. N.; Wang, H. W.; Zhang, X. H. et al. Bimetallic monolayer catalyst breaks the activity-selectivity trade-off on metal particle size for efficient chemoselective hydrogenations. *Nat. Catal.* **2021**, *4*, 840–849.

[3] Wang, Y.; Qin, R. X.; Wang, Y. K.; Ren, J.; Zhou, W. T.; Li, L. Y.; Ming, J.; Zhang, W. Y.; Fu, G.; Zheng, N. F. Chemoselective hydrogenation of nitroaromatics at the nanoscale iron(III)-OH-platinum interface. *Angew. Chem., Int. Ed.* **2020**, *59*, 12736–12740.

[4] Yang, F.; Wang, M. J.; Liu, W.; Yang, B.; Wang, Y.; Luo, J.; Tang, Y. S.; Hou, L. Q.; Li, Y.; Li, Z. H. et al. Atomically dispersed Ni as the active site towards selective hydrogenation of nitroarenes. *Green Chem.* **2019**, *21*, 704–711.

[5] Guo, C. Y.; Liang, C. H.; Qin, X. P.; Gu, Y. J.; Gao, P.; Shao, M. H.; Wong, W. T. Zeolitic imidazolate framework cores decorated with Pd nanoparticles and coated further with metal-organic framework shells (ZIF-8@Pd@MOF-74) as nanocatalysts for chemoselective hydrogenation reactions. *ACS Appl. Nano Mater.* **2020**, *3*, 7242–7251.

[6] Tian, S. B.; Hu, M.; Xu, Q.; Gong, W. B.; Chen, W. X.; Yang, J. R.; Zhu, Y. Q.; Chen, C.; He, J.; Liu, Q. et al. Single-atom Fe with Fe_1N_3 structure showing superior performances for both hydrogenation and transfer hydrogenation of nitrobenzene. *Sci. China Mater.* **2021**, *64*, 642–650.

[7] Li, L. Y.; Li, Y. X.; Jiao, L.; Liu, X. S.; Ma, Z. T.; Zeng, Y. J.; Zheng, X. S.; Jiang, H. L. Light-induced selective hydrogenation over PdAg nanocages in hollow MOF microenvironment. *J. Am. Chem. Soc.* **2022**, *144*, 17075–17085.

[8] Li, T. B.; Jian, X. Z.; Jiang, Q. K.; Qiao, B. T. Selective hydrogenation of nitroarenes by single-atom Pt catalyst through hydrogen transfer reaction. *Top. Catal.* **2022**, *65*, 1604–1608.

[9] Neeli, C. K. P.; Puthiaraj, P.; Lee, Y. R.; Chung, Y. M.; Baeck, S. H.; Ahn, W. S. Transfer hydrogenation of nitrobenzene to aniline in water using Pd nanoparticles immobilized on amine-functionalized UiO-66. *Catal. Today* **2018**, *303*, 227–234.

[10] Wu, W.; Zhang, W.; Long, Y.; Qin, J. H.; Ma, J. T. Different transfer hydrogenation pathways of halogenated nitrobenzenes catalyzed by Fe-, Co-, or Ni-based species confined in nitrogen doped carbon. *Mol. Catal.* **2020**, *497*, 111226.

[11] Chen, Z. X.; Song, J. T.; Zhang, R. R.; Li, R. L.; Hu, Q. K.; Wei, P. P.; Xi, S. B.; Zhou, X.; Nguyen, P. T. T.; Duong, H. M. et al. Addressing the quantitative conversion bottleneck in single-atom catalysis. *Nat. Commun.* **2022**, *13*, 2807.

[12] Jin, H. Q.; Li, P. P.; Cui, P. X.; Shi, J. A.; Zhou, W.; Yu, X. H.; Song, W. G.; Cao, C. Y. Unprecedentedly high activity and selectivity for hydrogenation of nitroarenes with single atomic Co_1-N_3P_1 sites. *Nat. Commun.* **2022**, *13*, 723.

[13] Zhang, G. J.; Tang, F. Y.; Wang, X.; Wang, L. Q.; Liu, Y. N. Atomically dispersed Co-S-N active sites anchored on hierarchically porous carbon for efficient catalytic hydrogenation of nitro compounds. *ACS Catal.* **2022**, *12*, 5786–5794.

[14] Cai, G. R.; Yan, P.; Zhang, L. L.; Zhou, H. C.; Jiang, H. L. Metal-organic framework-based hierarchically porous materials: Synthesis and applications. *Chem. Rev.* **2021**, *121*, 12278–12326.

[15] Sun, L. Z.; Lv, H.; Feng, J.; Guselnikova, O.; Wang, Y. Z.; Yamauchi, Y.; Liu, B. Noble-metal-based hollow mesoporous nanoparticles: Synthesis strategies and applications. *Adv. Mater.* **2022**, *34*, 2201954.

[16] Brown, C. M.; Lundberg, D. J.; Lamb, J. R.; Kevlishvili, I.; Kleinschmidt, D.; Alfaraj, Y. S.; Kulik, H. J.; Ottaviani, M. F.; Oldenhuis, N. J.; Johnson, J. A. Endohedrally functionalized metal-organic cage-cross-linked polymer gels as modular heterogeneous catalysts. *J. Am. Chem. Soc.* **2022**, *144*, 13276–13284.

[17] Tian, Z. B.; Dong, C.; Yu, Q.; Ye, R. P.; Duyar, M. S.; Liu, J.; Jiang, H. Q.; Wang, G. H. A universal nanoreactor strategy for scalable supported ultrafine bimetallic nanoparticles synthesis. *Mater. Today* **2020**, *40*, 72–81.

[18] Zhang, F. W.; Li, J. J.; Liu, P. Z.; Li, H.; Chen, S.; Li, Z. H.; Zan, W. Y.; Guo, J. J.; Zhang, X. M. Ultra-high loading single CoN_3 sites in N-doped graphene-like carbon for efficient transfer hydrogenation of nitroaromatics. *J. Catal.* **2021**, *400*, 40–49.

[19] Fan, Y. F.; Zhuang, C. F.; Li, S. J.; Wang, Y.; Zou, X. Q.; Liu, X. T.; Huang, W. M.; Zhu, G. S. Efficient single-atom Ni for catalytic transfer hydrogenation of furfural to furfuryl alcohol. *J. Mater. Chem. A* **2021**, *9*, 1110–1118.

[20] Chen, Y. J.; Ji, S. F.; Wang, Y. G.; Dong, J. C.; Chen, W. X.; Li, Z.; Shen, R. A.; Zheng, L. R.; Zhuang, Z. B.; Wang, D. S. et al. Isolated single iron atoms anchored on N-doped porous carbon as an efficient electrocatalyst for the oxygen reduction reaction. *Angew. Chem., Int. Ed.* **2017**, *56*, 6937–6941.

[21] Li, Y. X.; Lu, X. F.; Xi, S. B.; Luan, D. Y.; Wang, X.; Lou, X. W. Synthesis of N-doped highly graphitic carbon urchin-like hollow structures loaded with single-Ni atoms towards efficient CO_2 electroreduction. *Angew. Chem., Int. Ed.* **2022**, *61*, e202201491.

[22] Liu, W.; Feng, H. S.; Yang, Y. S.; Niu, Y. M.; Wang, L.; Yin, P.; Hong, S.; Zhang, B. S.; Zhang, X.; Wei, M. Highly-efficient RuNi single-atom alloy catalysts toward chemoselective hydrogenation of nitroarenes. *Nat. Commun.* **2022**, *13*, 3188.

[23] Sun, T.; Zang, W. J.; Yan, H.; Li, J.; Zhang, Z. Q.; Bu, Y. F.; Chen, W.; Wang, J.; Lu, J.; Su, C. L. Engineering the coordination environment of single cobalt atoms for efficient oxygen reduction and hydrogen evolution reactions. *ACS Catal.* **2021**, *11*, 4498–4509.

[24] Wu, F.; Pan, C.; He, C. T.; Han, Y. H.; Ma, W. J.; Wei, H.; Ji, W. L.; Chen, W. X.; Mao, J. J.; Yu, P. et al. Single-atom Co-N_4 electrocatalyst enabling four-electron oxygen reduction with enhanced hydrogen peroxide tolerance for selective sensing. *J. Am. Chem. Soc.* **2020**, *142*, 16861–16867.

[25] Zhang, J.; Zheng, C. Y.; Zhang, M. L.; Qiu, Y. J.; Xu, Q.; Cheong, W. C.; Chen, W. X.; Zheng, L. R.; Gu, L.; Hu, Z. P. et al. Controlling N-doping type in carbon to boost single-atom site Cu catalyzed transfer hydrogenation of quinoline. *Nano Res.* **2020**, *13*, 3082–3087.

[26] Zhao, C. X.; Liu, J. N.; Wang, J.; Wang, C. D.; Guo, X.; Li, X. Y.; Chen, X.; Song, L.; Li, B. Q.; Zhang, Q. A clicking confinement strategy to fabricate transition metal single-atom sites for bifunctional oxygen electrocatalysis. *Sci. Adv.* **2022**, *8*, eabn5091.

[27] Zhao, X.; Wang, F. L.; Kong, X. P.; Fang, R. Q.; Li, Y. W. Dual-metal hetero-single-atoms with different coordination for efficient synergistic catalysis. *J. Am. Chem. Soc.* **2021**, *143*, 16068–16077.

[28] Chen, Y. J.; Gao, R.; Ji, S. F.; Li, H. J.; Tang, K.; Jiang, P.; Hu, H. B.; Zhang, Z. D.; Hao, H. G.; Qu, Q. Y. et al. Atomic-level modulation of electronic density at cobalt single-atom sites derived from metal-organic frameworks: Enhanced oxygen reduction performance. *Angew. Chem., Int. Ed.* **2021**, *60*, 3212–3221.

[29] Chen, Y. J.; Jiang, B.; Hao, H. G.; Li, H. J.; Qiu, C. Y.; Liang, X.; Qu, Q. Y.; Zhang, Z. D.; Gao, R.; Duan, D. M. et al. Atomic-level regulation of cobalt single-atom nanozymes: Engineering high-efficiency catalase mimics. *Angew. Chem., Int. Ed.* **2023**, *62*, e202301879.

[30] Li, W. H.; Ye, B. C.; Yang, J. R.; Wang, Y.; Yang, C. J.; Pan, Y. M.; Tang, H. T.; Wang, D. S.; Li, Y. D. A single-atom cobalt catalyst for the fluorination of acyl chlorides at parts-per-million catalyst loading. *Angew. Chem., Int. Ed.* **2022**, *61*, e202209749.

[31] Chen, Y. Z.; Wang, C. M.; Wu, Z. Y.; Xiong, Y. J.; Xu, Q.; Yu, S. H.; Jiang, H. L. From bimetallic metal-organic framework to porous carbon: High surface area and multicomponent active dopants for excellent electrocatalysis. *Adv. Mater.* **2015**, *27*, 5010–5016.

[32] Guo, Y. C.; Liu, F.; Feng, L.; Wang, X. M.; Zhang, X.; Liang, J. S. Single Co atoms anchored on nitrogen-doped hierarchically ordered

porous carbon for selective hydrogenation of quinolines and efficient oxygen reduction. *Chem. Eng. J.* **2022**, *429*, 132150.

[33] Han, X. P.; Ling, X. F.; Wang, Y.; Ma, T. Y.; Zhong, C.; Hu, W. B.; Deng, Y. D. Generation of nanoparticle, atomic-cluster, and single-atom cobalt catalysts from zeolitic imidazole frameworks by spatial isolation and their use in zinc-air batteries. *Angew. Chem., Int. Ed.* **2019**, *58*, 5359–5364.

[34] Li, L.; Chen, Y. J.; Xing, H. R.; Li, N.; Xia, J. W.; Qian, X. Y.; Xu, H.; Li, W. Z.; Yin, F. X.; He, G. Y. et al. Single-atom Fe-N_5 catalyst for high-performance zinc-air batteries. *Nano Res.* **2022**, *15*, 8056–8064.

[35] Wang, Z.; Zhu, C.; Tan, H.; Liu, J.; Xu, L. L.; Zhang, Y. Q.; Liu, Y. P.; Zou, X. X.; Liu, Z.; Lu, X. H. Understanding the synergistic effects of cobalt single atoms and small nanoparticles: Enhancing oxygen reduction reaction catalytic activity and stability for zinc-air batteries. *Adv. Funct. Mater.* **2021**, *31*, 2104735.

[36] Wu, C.; Zhu, C. Y.; Liu, K. K.; Yang, S. W.; Sun, Y.; Zhu, K.; Cao, Y. L.; Zhang, S.; Zhuo, S. F.; Zhang, M. et al. Nano-pyramid-type Co-ZnO/NC for hydrogen transfer cascade reaction between alcohols and nitrobenzene. *Appl. Catal. B* **2022**, *300*, 120288.

[37] Zhou, B. J.; Liu, Y. Y.; Wu, X. L.; Liu, H.; Liu, T.; Wang, Y.; Mehdi, S.; Jiang, J. C.; Li, B. J. Wood-derived integrated air electrode with Co-N sites for rechargeable zinc-air batteries. *Nano Res.* **2022**, *15*, 1415–1423.

[38] Li, X.; Surkus, A. E.; Rabeah, J.; Anwar, M.; Dastigir, S.; Junge, H.; Brückner, A.; Beller, M. Cobalt single-atom catalysts with high stability for selective dehydrogenation of formic acid. *Angew. Chem., Int. Ed.* **2020**, *59*, 15849–15854.

[39] Wang, X. X.; Cullen, D. A.; Pan, Y. T.; Hwang, S.; Wang, M. Y.; Feng, Z. X.; Wang, J. Y.; Engelhard, M. H.; Zhang, H. G.; He, Y. H. et al. Nitrogen-coordinated single cobalt atom catalysts for oxygen reduction in proton exchange membrane fuel cells. *Adv. Mater.* **2018**, *30*, 1706758.

[40] Xie, W. F.; Song, Y. K.; Li, S. J.; Li, J. B.; Yang, Y. S.; Liu, W.; Shao, M. F.; Wei, M. Single-atomic-Co electrocatalysts with self-supported architecture toward oxygen-involved reaction. *Adv. Funct. Mater.* **2019**, *29*, 1906477.

[41] Yin, P. Q.; Yao, T.; Wu, Y.; Zheng, L. R.; Lin, Y.; Liu, W.; Ju, H. X.; Zhu, J. F.; Hong, X.; Deng, Z. X. et al. Single cobalt atoms with precise N-coordination as superior oxygen reduction reaction catalysts. *Angew. Chem., Int. Ed.* **2016**, *55*, 10800–10805.

[42] Doustkhah, E.; Hassandoost, R.; Khataee, A.; Luque, R.; Assadi, M. H. N. Hard-templated metal-organic frameworks for advanced applications. *Chem. Soc. Rev.* **2021**, *50*, 2927–2953.

[43] Feng, B. B.; Guo, R.; Cai, Q. L.; Song, Y. P.; Li, N.; Fu, Y. H.; Chen, D. L.; Zhang, J. W.; Zhu, W. D.; Zhang, F. M. Construction of isolated Ni sites on nitrogen-doped hollow carbon spheres with Ni-N_3 configuration for enhanced reduction of nitroarenes. *Nano Res.* **2022**, *15*, 6001–6009.

[44] Guan, B. Y.; Yu, L.; Lou, X. W. Formation of single-holed cobalt/N-doped carbon hollow particles with enhanced electrocatalytic activity toward oxygen reduction reaction in alkaline media. *Adv. Sci.* **2017**, *4*, 1700247.

[45] Yang, H. Z.; Wang, X. Secondary-component incorporated hollow MOFs and derivatives for catalytic and energy-related applications. *Adv. Mater.* **2019**, *31*, 1800743.

[46] Yang, Q. H.; Yang, C. C.; Lin, C. H.; Jiang, H. L. Metal-organic-framework-derived hollow N-doped porous carbon with ultrahigh concentrations of single Zn atoms for efficient carbon dioxide conversion. *Angew. Chem., Int. Ed.* **2019**, *58*, 3511–3515.

[47] Ye, C. L.; Chen, X. J.; Li, S. S.; Feng, B. B.; Fu, Y. H.; Zhang, F. M.; Chen, D. L.; Zhu, W. D. PdZn intermetallic compound stabilized on ZnO/nitrogen-decorated carbon hollow spheres for catalytic semihydrogenation of alkynols. *Nano Res.* **2022**, *15*, 3090–3098.

[48] Zhang, F.; Wei, Y. Y.; Wu, X. T.; Jiang, H. Y.; Wang, W.; Li, H. X. Hollow zeolitic imidazolate framework nanospheres as highly efficient cooperative catalysts for [3 + 3] cycloaddition reactions. *J. Am. Chem. Soc.* **2014**, *136*, 13963–13966.

[49] Li, J. J.; Xia, W.; Tang, J.; Gao, Y.; Jiang, C.; Jia, Y. N.; Chen, T.; Hou, Z. F.; Qi, R. J.; Jiang, D. et al. Metal-organic framework-derived graphene mesh: A robust scaffold for highly exposed Fe-N_4 active sites toward an excellent oxygen reduction catalyst in acid media. *J. Am. Chem. Soc.* **2022**, *144*, 9280–9291.

[50] Han, X.; Zhang, T. Y.; Wang, X. H.; Zhang, Z. D.; Li, Y. P.; Qin, Y. J.; Wang, B. Q.; Han, A. J.; Liu, J. F. Hollow mesoporous atomically dispersed metal-nitrogen-carbon catalysts with enhanced diffusion for catalysis involving larger molecules. *Nat. Commun.* **2022**, *13*, 2900.

[51] Lee, G.; Na, W.; Kim, J.; Lee, S.; Jang, J. Improved electrochemical performances of MOF-derived Ni-Co layered double hydroxide complexes using distinctive hollow-in-hollow structures. *J. Mater. Chem. A* **2019**, *7*, 17637–17647.

[52] Yu, L.; Yang, J. F.; Lou, X. W. Formation of CoS_2 nanobubble hollow prisms for highly reversible lithium storage. *Angew. Chem., Int. Ed.* **2016**, *55*, 13422–13426.

[53] Zhang, J. T.; Zhang, L. P.; Wang, X. D.; Zhu, W.; Zhuang, Z. B. A hierarchical hollow-on-hollow NiCoP electrocatalyst for efficient hydrogen evolution reaction. *Chem. Commun.* **2020**, *56*, 90–93.

[54] Zhang, X. F.; Wang, Z. G.; Ding, M. L.; Feng, Y.; Yao, J. F. Advances in cellulose-metal organic framework composites: Preparation and applications. *J. Mater. Chem. A* **2021**, *9*, 23353–23363.

[55] Cui, J.; Xu, X. R.; Yang, L. Y.; Chen, C. T.; Qian, J. S.; Chen, X.; Sun, D. P. Soft foam-like UiO-66/polydopamine/bacterial cellulose composite for the removal of aspirin and tetracycline hydrochloride. *Chem. Eng. J.* **2020**, *395*, 125174.

[56] Chen, M. W.; Liu, T.; Zhang, X. B.; Zhang, R. Q.; Tang, S.; Yuan, Y. H.; Xie, Z. J.; Liu, Y. J.; Wang, H.; Fedorovich, K. V. et al. Photoinduced enhancement of uranium extraction from seawater by MOF/black phosphorus quantum dots heterojunction anchored on cellulose nanofiber aerogel. *Adv. Funct. Mater.* **2021**, *31*, 2100106.

[57] Abramova, A.; Couzon, N.; Leloire, M.; Nerisson, P.; Cantrel, L.; Royer, S.; Loiseau, T.; Volkringer, C.; Dhainaut, J. Extrusion-spheronization of UiO-66 and UiO-66_NH_2 into robust-shaped solids and their use for gaseous molecular iodine, xenon, and krypton adsorption. *ACS Appl. Mater. Interfaces* **2022**, *14*, 10669–10680.

[58] Ni, W. P.; Liu, Z. X.; Guo, X. G.; Zhang, Y.; Ma, C.; Deng, Y. J.; Zhang, S. G. Dual single-cobalt atom-based carbon electrocatalysts for efficient CO_2-to-syngas conversion with industrial current densities. *Appl. Catal. B* **2021**, *291*, 120092.

[59] Wu, J. B.; Zhou, H.; Li, Q.; Chen, M.; Wan, J.; Zhang, N.; Xiong, L. K.; Li, S.; Xia, B. Y.; Feng, G. et al. Densely populated isolated single Co-N site for efficient oxygen electrocatalysis. *Adv. Energy Mater.* **2019**, *9*, 1900149.

[60] Zhang, F.; Ma, J.; Tan, Y.; Yu, G.; Qin, H. X.; Zheng, L. R.; Liu, H. B.; Li, R. Construction of porphyrin porous organic cage as a support for single cobalt atoms for photocatalytic oxidation in visible light. *ACS Catal.* **2022**, *12*, 5827–5833.

[61] Zhu, Y. Q.; Sun, W. M.; Chen, W. X.; Cao, T.; Xiong, Y.; Luo, J.; Dong, J. C.; Zheng, L. R.; Zhang, J.; Wang, X. L. et al. Scale-up biomass pathway to cobalt single-site catalysts anchored on N-doped porous carbon nanobelt with ultrahigh surface area. *Adv. Funct. Mater.* **2018**, *28*, 1802167.

[62] Fei, H. F.; Long, Y. D.; Yu, H. J.; Yavitt, B. M.; Fan, W.; Ribbe, A.; Watkins, J. J. Bimodal mesoporous carbon spheres with small and ultra-large pores fabricated using amphiphilic brush block copolymer micelle templates. *ACS Appl. Mater. Interfaces* **2020**, *12*, 57322–57329.

[63] Shen, W. Z.; Hu, T. P.; Fan, W. B. Cellulose generated-microporous carbon nanosheets with nitrogen doping. *RSC Adv.* **2014**, *4*, 9126–9132.

[64] Wang, F. X.; Liang, L.; Shi, L.; Liu, M. S.; Sun, J. M. CO_2-assisted synthesis of mesoporous carbon/C-doped ZnO composites for enhanced photocatalytic performance under visible light. *Dalton Trans.* **2014**, *43*, 16441–16449.